Available online at www.sciencedirect.com
ScienceDirect
Remote Sensing of Environment 112 (2008) 2455–2468
Remote Sensing of Environment
www.elsevier.com/locate/rse

Aerosol retrieval over ocean from SEVIRI for the use in GERB Earth's radiation budget analyses ☆

Bart De Paepe [a,c,*], Alexander Ignatov [b], Steven Dewitte [a,c], Alessandro Ipe [a]

[a] *Royal Meteorological Institute of Belgium, Department of Observations, Section Remote Sensing from Space, Brussels, Belgium*
[b] *NOAA/NESDIS/Office of Research and Applications, Camp Springs, Maryland, USA*
[c] *Vrije Universiteit Brussel, Faculty of Engineering, Brussels, Belgium*

Received 12 June 2007; received in revised form 26 September 2007; accepted 17 November 2007

Abstract

To study the effect of aerosols on the Earth's radiation budget (ERB), the Royal Meteorological Institute of Belgium (RMIB) has integrated spectral aerosol optical depth (AOD) measurements over the ocean from the Spinning Enhanced Visible and Infra-Red Scanner (SEVIRI) into its Geostationary Earth's Radiation Budget, or GERB, processing system referred to as the RGP. Aerosols affect the ERB both directly (when radiation interacts with an aerosol particle) and indirectly (when aerosols act as cloud condensation nuclei). Quantifying the indirect effect is challenging as it requires accurate aerosol retrievals in the close proximity to clouds, where aerosol retrievals may be biased due to leakages from the cloud mask (CM). The initial focus of the RGP project was on the direct effect using confidently clear scenes.

A single channel CM exploiting the SEVIRI temporal sampling was developed at the RMIB for the use in the RGP project. In this study, that single channel mask was evaluated against two multi-channel CMs, one from the Meteorological Products Extraction Facility (MPEF) at the European Organization for the Exploitation of Meteorological Satellites (EUMETSAT), and the other from the Satellite Application Facility for Supporting NoWCasting and Very Short Range Forecasting (SAFNWC), respectively. The NOAA/NESDIS Advanced Very High Resolution Radiometer (AVHRR) single channel aerosol algorithm was adjusted to SEVIRI spectral bands and consistently applied to the pixels identified as cloud-free. The aerosol products corresponding to the three CMs were compared, and the RMIB CM was found to be sufficiently accurate and conservative, for RGP applications.

Comparisons with independent AODs derived from the MODerate resolution Imaging Spectroradiometer (MODIS) onboard Terra and Aqua satellites show that the RMIB CM-based SEVIRI aerosol product compares well with its MODIS counterpart. However, a small fraction of cloud-contaminated pixels may still remain in the SEVIRI AOD imagery, chiefly within one to two SEVIRI pixels of the cloud boundary, thus limiting its use for indirect forcing studies. Also, the RMIB CM may screen high AOD non-dust aerosol events (e.g., smoke from biomass burning) as cloud. The potential of the new SEVIRI aerosol product is illustrated by generating 9 km-resolution seasonal maps of AODs and Ångström Exponents, and by using the GERB radiative flux measurements for a preliminary quick assessment of the direct aerosol forcing.

Keywords: Aerosol optical depth; SEVIRI; Cloud screening; Direct radiative effect

☆ Special thanks go to the RMIB GERB Team for providing the GERB data and for their support during processing; to Yury Kihai from NOAA/NESDIS for his dedicated collaboration during the NESDIS algorithm implementation in the RGP; to the SAFNWC for supplying their software, to Didier Tanré, Sergio Pugnaghi and Renato Santangelo for establishing and maintaining the Capo Verdo and Lampedusa AERONET sites; and to Ms. Alison Smith for help with technical editing. This paper would not have been possible without the excellent data services of EUMETSAT, RMIB, ECMWF and NASA EOS Data Gateway. This research is funded by the Belgian Science Policy and hosted by the RMIB. A. Ignatov was funded under the NASA EOS/CERES (NASA contract L-90987C) and GOES-R Algorithm Working Group Projects. The views, opinions, and findings contained in this report are those of the authors and should not be construed as an official NASA, NOAA or U.S. Government position, policy, or decision.

* Corresponding author. Royal Meteorological Institute of Belgium, Department of Observations, Section Remote Sensing from Space, Building B, Ringlaan 3, 1180 Brussels.
E-mail address: bart.depaepe@oma.be (B. De Paepe).

0034-4257/$ - see front matter © 2007 Elsevier Inc. All rights reserved.
doi:10.1016/j.rse.2007.11.005

1. Introduction

The Meteosat-8 satellite launched in 2002 carries the Geostationary Earth's Radiation Budget (GERB; Harries et al. (2005)) instrument onboard. In the past, Earth's Radiation Budget (ERB) instruments such as the Clouds and the Earth's Radiant Energy System (CERES) have been flown onboard polar orbiting platforms (Wielicki et al., 1996). The GERB is the first ERB instrument onboard a geostationary platform. The Royal Meteorological Institute of Belgium (RMIB) is in charge of operational processing of the GERB data in near-real time, and delivering products to the community for scientific studies (Dewitte et al., accepted for publication).

Meteosat-8 also hosts the Spinning Enhanced Visible and Infra-Red Imager (SEVIRI) (Schmetz et al., 2002). SEVIRI provides imagery products in 12 spectral bands, three of which are spectrally close to the respective solar reflectance bands (SB) of the Advanced Very High Resolution Radiometer (AVHRR) used for aerosol retrievals over oceans (Brindley & Ignatov, 2006). The 15-minute temporal sampling of the full disk, at 5-km spatial resolution and 3-km scan increment at nadir (Schmetz et al., 2002), makes SEVIRI particularly attractive for aerosol mapping over oceans, in the Meteosat domain.

The effect of aerosols on the ERB is highly uncertain (King et al., 1999). The major objective of this study is to document the aerosol retrievals from SEVIRI, which have been recently added to the RMIB GERB processing project, known as the RGP, to complement the GERB fluxes.

Aerosols affect ERB both directly and indirectly, in the latter case through the aerosol particles acting as nuclei for the formation of cloud droplets (e.g., Coakley and Walsch, 2002; Loeb and Kato, 2002). There is an implicit difficulty in the measurement of the indirect radiative effect from space because, in the vicinity of clouds, the hygroscopic growth of aerosol particles may be indistinguishable from aerosol retrieval artifacts. Residual cloud in the field of view or cloud ambience or a three-dimensional effect can all lead to a seemingly elevated retrieved AOD (e.g., Matheson et al., 2005; Wen et al., 2006). As a result, a loose cloud screening would lead to an overestimation of the indirect effect of aerosols, whereas an overly conservative screening may remove clear aerosol pixels, thus leading to an underestimation of the indirect aerosol effect.

More research is needed to define accurate cloud screening strategies that would allow analyses of the aerosol indirect forcing from satellite retrievals. The first focus of the RGP was thus to generate a "clean" aerosol product, using a conservative cloud mask (CM), and append this aerosol product to the GERB fluxes for use in direct forcing analyses. A simple yet conservative CM was developed at the RMIB. To evaluate the performance of the RMIB CM with the aerosol product, two other CMs were implemented in the RGP processing developed by the Meteorological Products Extraction Facility (MPEF) at the European Organization for the Exploitation of Meteorological Satellites (EUMETSAT) and by the Satellite Application Facility for Supporting NoWCasting and Very Short Range Forecasting (SAFNWC), respectively. Their respective aerosol products were then compared with the RMIB CM. This study documents the results of these comparisons and substantiates the choice to use the RMIB CM for the operational RGP.

This study first validates the AOD retrieval algorithm using confidently clear SEVIRI pixels and describes the selected CMs and their performance with the aerosol product. These analyses form the basis for selecting the simple and conservative RMIB CM for the RGP. The study then evaluates the long-term performance of RMIB CM-based aerosol product by analyzing one year of AOD retrievals, and comparing those results with independent MODIS aerosol retrievals (collection 5) obtained from the NASA archives.

2. NOAA/NESDIS AVHRR aerosol algorithm and its validation against AERONET under confidently cloud-free conditions

Three AODs at 0.63, 0.83 and 1.61 μm are derived from the respective SEVIRI bands, independently, using the NOAA/NESDIS third-generation algorithm documented in Ignatov and Stowe (2002). This algorithm was modified for the three SEVIRI SB as described in Brindley and Ignatov (2006). The single channel algorithm assumes that the aerosol type and ocean diffuse reflectance are globally non-variable. For a given sun-view geometry, it attributes all variability in the top-of-atmosphere radiances to only one parameter, AOD.

Inputs to the three look-up-tables are the so-called NOAA albedos, A_i (Ignatov & Stowe, 2002). For SEVIRI, they are derived from level 1.5 counts converted to radiances L_i (in $Wm^{-2}sr^{-1}$ μm^{-1}) following the calibration of Govaerts and Clerici (2004). The "one input–one output" approach adopted in NESDIS single channel retrievals lends itself to an independent check of the radiometric performance of individual SEVIRI bands using the derived AOD product. This is particularly important for AVHRR and SEVIRI, whose SB are lacking an onboard calibration device and are therefore calibrated vicariously. By combining the three AODs, Ångström Exponent (AE) parameters related to particle size can also be estimated. The AE is even more sensitive to calibration errors than AOD.

This simple algorithm has been extensively tested with data from different platforms and sensors and, invariably, it has shown robust and predictable performance. Currently, the third generation of this algorithm is used at NOAA/NESDIS to make operational aerosol retrievals from AVHRR/3 onboard NOAA-16, -17, -18, and MetOp-A. This algorithm has also been adopted by the CERES project to generate a primary aerosol product from the Visible Infra-Red Scanner (VIRS) onboard the Tropical Rainfall Measuring Mission (TRMM) satellite and a back-up aerosol product from the MODIS instrument onboard the Terra and Aqua satellites (Ignatov et al., 2006). Using the same aerosol algorithm in the GERB processing provides for consistency with its CERES counterpart. Based on prior empirical analyses, the AVHRR-like retrievals are restricted to solar and view zenith angles less than 60° and sun glint angles greater than 40°.

AVHRR-like aerosol retrievals from SEVIRI have already been generated and validated against AERONET using a few

Table 1
AERONET locations that are used for comparison in our analysis

Cape Verde	16.73°N	22.94°W
Lampedusa	35.52°N	12.63°E

dust case studies in Brindley and Ignatov (2006). For the RGP, however, the algorithm was implemented independently and operationally applied to much larger data sets, which therefore requires further evaluation. Two AERONET oceanic stations listed in Table 1 have been identified for the use in this validation. The most complete production of level 2.0 AERONET data for these stations commenced in early March 2004. For the SEVIRI aerosol retrievals to cover the full diurnal cycle at any location, these locations must avoid both sun glint and clouds for the entire day. We have identified several days for which the RMIB, MPEF and SAFNWC CMs all indicate cloud-free conditions over these stations by visual analyses of the satellite images.

Fig. 1 shows SEVIRI versus AERONET comparisons for four days in March 2004. The point AERONET observations are compared to SEVIRI retrievals and averaged over the nearest available ocean pixels. For the island sites, this comprises 10 SEVIRI pixels either side of the ground station where the land pixels have been removed. This roughly corresponds to a region of 60×60 km. For the comparisons, the AERONET AODs, measured at the wavelengths of 0.675 and 0.87 μm, were scaled to the SEVIRI reference wavelengths, 0.63 and 0.83 μm, using an Ångström fit presented in Eq. (1).

$$\frac{\tau(\lambda)}{\tau_0} = \left(\frac{\lambda_0}{\lambda}\right)^{\alpha} \sim 1.01 \tag{1}$$

Where τ is the AOD, λ the wavelength, and α the AE. At Cape Verde, AOD on March 5 to 7, 2004, is high due to the dust event over the Sahara. (Note that Fig. 1a is an independent reproduction of Fig. 9a in Brindley and Ignatov (2006) On all three days, the SEVIRI time series are smoother than the AERONET, presumably due to the spatial averaging, and SEVIRI reads lower AODs than AERONET. The average bias is from 0.05 to 0.10 with a maximum of ~0.2 to 0.3. The low bias in SEVIRI retrievals and its diurnal cycle suggest that the globally average aerosol type, assumed in the NESDIS third-generation algorithm, does not fully represent the aerosol type at the Cape Verde site in March 2004, what also could explain the bias of 15 to 25% between SEVIRI and AERONET. Further we observe a shift between the time series of SEVIRI and AERONET, where the peaks can be separated up to 2 h. This is due to the spatial averaging we perform to obtain the SEVIRI value.

At Lampedusa, AOD<0.1 correspond to background maritime values. Here SEVIRI reads higher AODs than AERONET. The bias is ~+0.015 at 0.63 μm and ~+0.03 at 0.83 μm and is likely due to errors in SEVIRI retrievals as AERONET AOD is typically accurate to within <±0.02 (Smirnov et al., 2000).

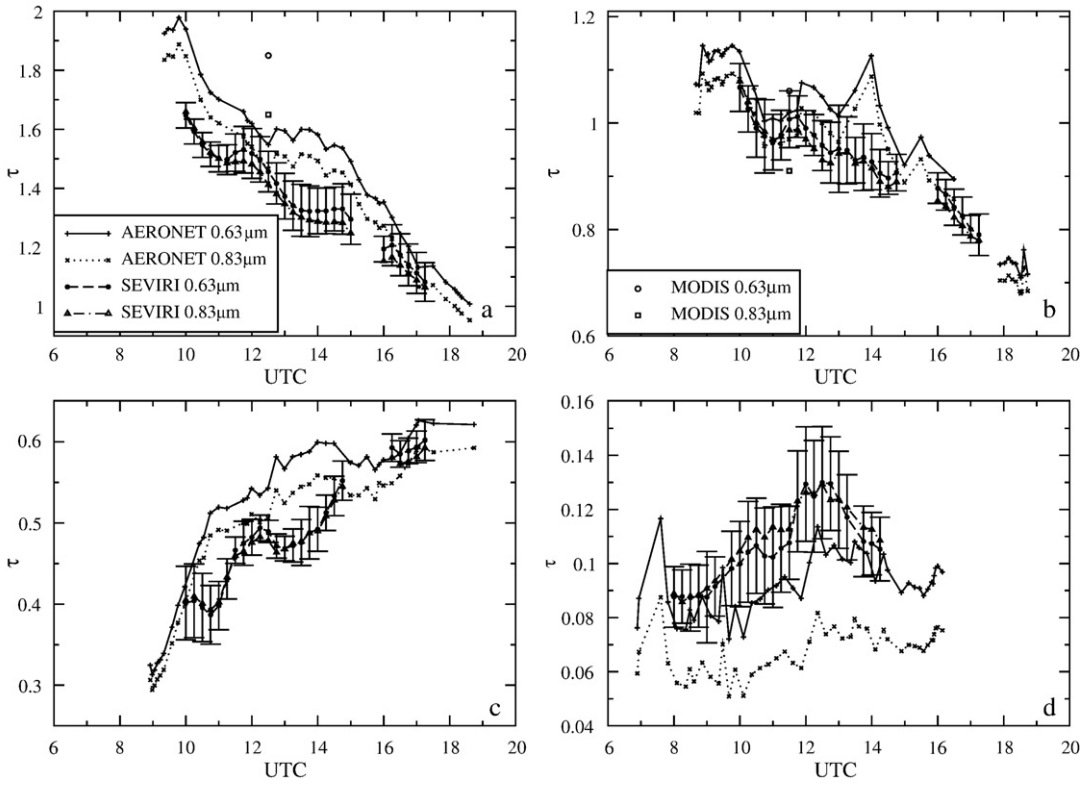

Fig. 1. Diurnal variation of SEVIRI and AERONET at $\tau_{0.63}$ and $\tau_{0.83}$: a, b, and c are at Cape Verde on March 5, 6, and 7, 2004, respectively; d is at Lampedusa on March 12, 2004. The error bars are for SEVIRI at 0.63 μm, and are indicative for 0.83 μm as well.

Satellite retrievals at low AODs are mostly sensitive to errors in either sensor calibration or ocean reflectance and much less sensitive to the aerosol model (e.g., Ignatov et al. (2006) and references therein). Elevated surface reflectance is possible in coastal waters and unlikely near Lampedusa Island, where Mediterranean Case 1 waters are very clean. A calibration error of ~+2% in band 1 and ~+10% in band 2 may explain the observed biases. More analyses are needed to determine the root cause of these SEVIRI aerosol biases in the panels of Fig. 1.

Available MODIS retrievals are also superimposed in Fig. 1. No Aqua data was available on either day within the spatial window of ~60 km adopted in this study, and Terra was only reporting aerosol data on March 5 and 6, 2004. This data availability illustrates the overwhelming superiority in local coverage from a geostationary platform. Interestingly, in both cases, when MODIS retrievals were available, the SEVIRI retrievals are closer to the AERONET measurements in both bands.

3. RMIB cloud mask and its evaluation against MPEF and SAFNWC cloud masks

3.1. Three cloud masks used in this study

This section provides a description of the RMIB CM, and a brief summary of the other two algorithms. For more detailed information, refer to the corresponding references. The emphasis below is on the cloud screening over ocean, but all three CMs are capable of working over land as well, using a different set of algorithms and tests.

3.1.1. RMIB CM

The RMIB CM is based on comparison of measured top-of-atmosphere reflectance with theoretically calculated look-up-tables, for various surface reflectances, cloud phases, scene geometries, and cloud optical depths (Nakajima & King, 1990). The look-up-tables were generated using the STREAMER (Key & Schweiger, 1998) radiative transfer model (RTM) for a limited set of ideal scenes, including five Lambertian surfaces (of which one type represents ocean), two phases (liquid and ice), and one uniform cloud layer with cloud optical depths τ ranging from 0 to 128, by series of 0, 0.01, 0.02, 0.04, 0.07, 0.1, 0.2, 0.4, 0.7, 1, 2, 4, 7, 10, 20, 40, 70, 100, 128. As shown in Nakajima and Nakajima (1995), there is an empirical relation between the reflectances and the cloud optical depth, which is merely insensitive to cloud particle size in the visible wavelengths. By rescaling this law between 0 and 1, according to the mean cloud amount for each visible channel λ, one obtains:

$$C_\lambda(\theta_0,\theta,\varphi,\alpha,\text{phase},\tau) = \frac{\rho_\lambda(\theta_0,\theta,\varphi,\alpha,\text{phase},\tau)-\rho_\lambda(\theta_0,\theta,\varphi,\alpha,\tau=0)}{\rho_\lambda(\theta_0,\theta,\varphi,\text{phase},\tau=128)-\rho_\lambda(\theta_0,\theta,\varphi,\alpha,\tau=0)} \quad (2)$$

where τ=0 represents clear sky conditions above the ground surface, and τ=128 represents a fully opaque cloudy conditions (note that the upper limit was selected for consistency with CERES). Here, θ_0 is the solar zenith angle, θ is the view zenith angle, φ is the relative azimuth angle, and phase is the cloud thermodynamical phase. Due to the specific shape of these curves, the LUTs can be parameterized using a modified sigmoid function of the logarithm of the optical depth (for more details, see Ipe et al. (2004)).

For each SEVIRI pixel the noniterative algorithm is applied as follows:

(1) Assign the surface geotype according to a static surface type map (identical to that adopted in CERES, Loeb et al. (2003)).
(2) Compute the cloud thermodynamic phase using a fixed threshold on the 10.8 μm brightness temperature.
(3) Select the solar visible channel with the largest contrast between opaque clouds and clear sky radiances. The contrast is given by the denominator of Eq. (2). The selected channel is 0.8 μm for ocean and 0.6 μm for other surfaces. ρ_λ (θ_0, θ, φ, α, τ=0) (Ipe et al., 2003) is the composite clear sky radiance, ρ_λ (θ_0, θ, φ, phase, τ=128) is the opaque cloud value calculated by an RTM.
(4) For this channel, compute the mean cloud amount C according to Eq. (2), and estimate the associated cloud optical depth.
(5) Flag a pixel as cloudy if its derived cloud optical depth is above a threshold value (typically, 0.6).
(6) Apply the Brindley–Russel dust detection algorithm. To reduce the risk for this CM to identify thick aerosols with AOD >~0.6 (mineral aerosol, biomass burning, volcanic plumes) as cloud, Brindley and Russel (2006) developed a dust detection algorithm over ocean. Using this algorithm, dusty pixels erroneously flagged as "cloud" by the RMIB CM are restored and appended to the clear sky pixels identified by prior tests. Empirical analysis shows that most of the dust aerosols are initially detected as cloud, but then successfully restored back to clear sky by the Brindley–Russel test. However, non-dust aerosols with high AOD (e.g., biomass burning) may still be screened out by the current CM, potentially leading to a low bias in non-dust AODs.
(7) Perform a spectral test. Since the RMIB CM is based on the solar channels, it can miss small cloudy features, cirrus clouds, or other thin features such as contrails, which do not reflect very brightly in the visible channels. To detect them, an additional empirically derived spectral test is performed based on use of the brightness temperatures (T) of the thermal channels at 10.8, and 12.0 μm:

$$\begin{aligned} &297\text{K} \le 11\times T_{10.8} - 10\times T_{12.0} \le 313\text{K} \\ &T_{12.0} \le 278\text{K}. \end{aligned} \quad (3)$$

Pixels that satisfy these two conditions are flagged as "cloud" and excluded from aerosol retrievals.

3.1.2. MPEF CM

The cloud processing for Meteosat-8 is based on a multispectral threshold technique described in Lutz (1999). The first two tests compare SEVIRI reflectances in individual bands and their differences, with thresholds. The next two tests compare

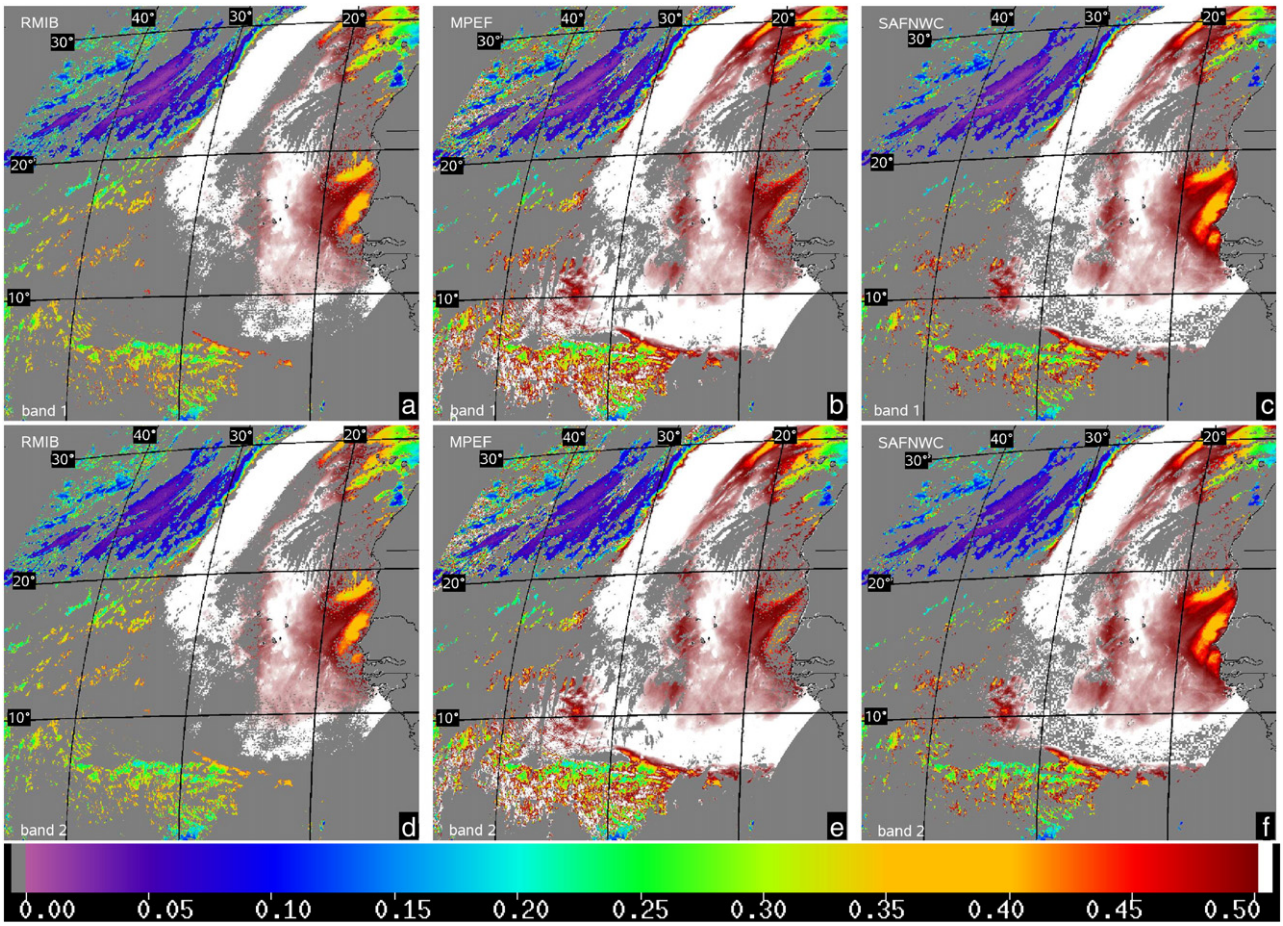

Fig. 2. SEVIRI AOD on March 6, 2004 at 12:00 UTC using RMIB CM (first column; a,d); MPEF CM (second column; b,e); and SAFNWC CM (third column; c,f). First row (a,b,c) is for band 1 (0.63 μm), τ 0.63; and second row (d,e,f,) is for band2 (0.83 μm), τ 0.83. Grey color indicates "no retrievals" (due to cloud, land, glint, etc.), and white color corresponds to AOD>0.5.

threshold brightness temperatures and their differences, respectively. The fifth test is a threshold on standard deviation of both solar and thermal channels. Two final tests on sun glint and on snow and ice complete the scene identification algorithm.

The MPEF CM is disseminated in near-real time and can also be obtained from the EUMETSAT Unified Meteorological Archive and Retrieval Facility. Please note that ongoing improvements in the MPEF CM algorithm (Meteorological Products Extraction Facility, 2007) do not trigger reprocessing of the archive. As a result, the EUMETSAT data used in this study reflect the status of the MPEF CM effective as of 2004.

3.1.3. SAFNWC CM

The SAFNWC CM is also based on a multi-spectral thresholding technique (Derrien & Le Gléau, 2005). A first sequence of tests allows the identification of pixels contaminated by clouds, snow or ice. The sequence of tests depends on the illumination conditions (daytime, nighttime, twilight, or sun glint) and surface type (land or ocean). Most of the thresholds in the thermal IR bands are dynamically determined, for each view geometry, using RTM simulations with numerical weather prediction model forecast parameters and ancillary data. Finally, a spatial uniformity test is applied.

In the RGP data stream, the SAFNWC CM was acquired by running the SAFNWC software using European Centre for Medium-Range Weather Forecast model input data.

3.2. Relative performance of the three CMs

Fig. 2 shows the AOD retrievals over the North Atlantic on March 6, 2004 at 12:00 UTC. Rows represent different bands (0.63 μm, and 0.83 μm) and columns different CMs (RMIB, MPEF and SAFNWC). The differences between the CMs are significant. The number of clouds detected by the CM (defined by the fraction of grey in Fig. 2) is highest for the RMIB and lowest for the MPEF CM, with the SAFNWC falling in between the two.

To facilitate the evaluation of the relative efficacy of different CMs, in particular their ability to separate cloud from dust, Fig. 3 plots the corresponding true-color (in plate a), the CM RGB images (in plate b), and the corresponding statistics (in plate c). Apart from the white areas, where all 3 CMs indicate "cloud", and black areas where all 3 CMs indicate "clear", the other prevalent colors are red, where the RMIB CM indicates "cloud" but the MPEF and the SAFNWC CMs indicate "clear", and magenta, where the RMIB and the SAFNWC CMs indicate

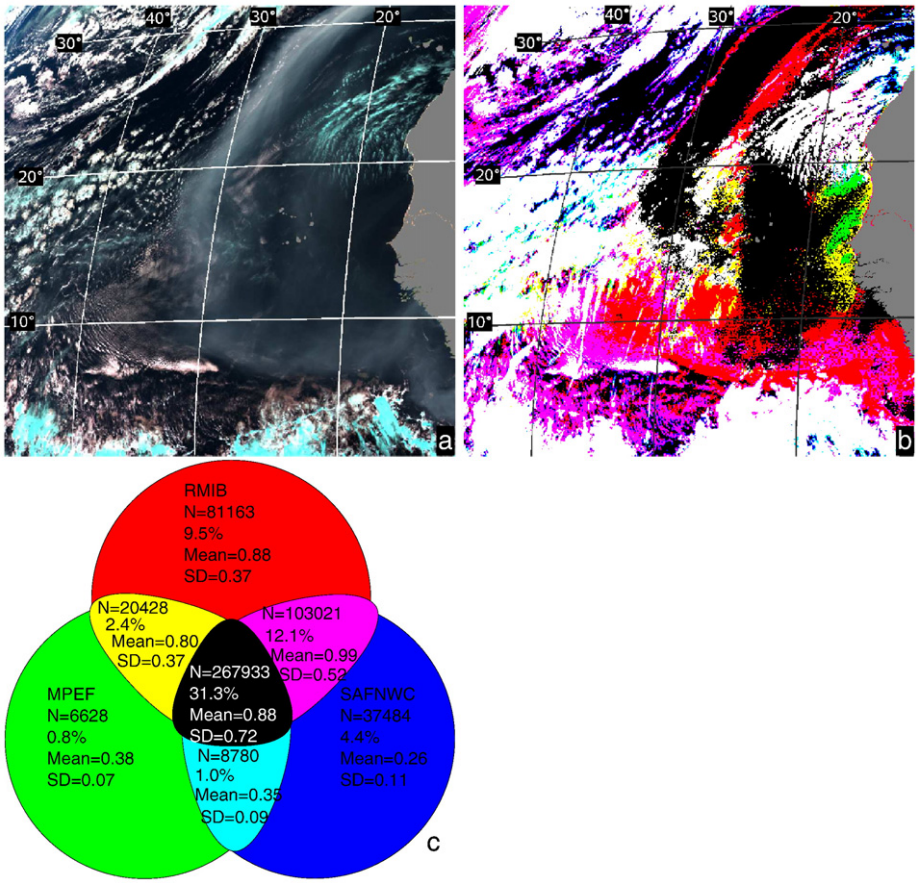

Fig. 3. Scene analysis March 6, 2004 at 12:00 UTC: (a) RGB (IR 1.6 μm, VIS 0.8 μm, VIS 0.6 μm); (b) RGB (RMIB CM, MPEF CM, SAFNWC CM); (c) statistics for plate (b).

"cloud" but the MPEF CM indicates "clear". Comparing this image with the true-color image suggests that, in this particular case, the RMIB CM identifies some dusty areas as cloud (e.g., at about 9°N and 20°–30°W. On the other hand, the magenta from 6°–7°N and 20°–30°W appears to be real cloud that has not been detected by the MPEF CM.

Concentrating on the area south of 10°N and west of 30°W on Fig. 2, the MPEF CM and, to a smaller extent, the SAFNWC CMs, flag a number of pixels in the vicinity of cloud borders as cloud-free, with elevated and spectrally neutral AODs. These are likely residual cloud. On the other hand, the RMIB CM-based AODs are spatially more uniform here and decrease with wavelength as expected (in contrast to the spectrally neutral cloud signal). The statistics on Fig. 3 (plate c) support these observations. The red area has a mean AOD of 0.88, against the low AOD of the green, cyan, and blue regions. The center of the image on Fig. 2 seems to support the expectation that in high AOD areas, the RMIB CM may be overly conservative.

To attach a quantitative measure to the above observations, Fig. 4 plots AODs and AEs as a function of proximity to the cloud border. All three CMs show an increase in AOD and a decrease in AE as one approaches cloud. Part of this effect may be due to the swelling of aerosols closer to the clouds, and part may be due to artifacts of retrievals. However, none of these factors can explain the difference in AOD between the CMs at identical distances, which can only be attributed to the CMs themselves. This is important with respect to our choice of a cloud mask for assessing the direct aerosol effect.

The overall performance of the RMIB CM is comparable to that of the SAFNWC CM, except at the distance = 1 pixel, where the RMIB AOD is biased high by ~+0.05 with respect to the SAFNWC AOD. The corresponding RMIB AE is biased low by 0.02–0.03 compared to the SAFNWC, indicating somewhat larger residual cloud contamination in the RMIB product, at all distances. Large cloud particles flatten out the spectral dependence of AOD and therefore reduce the AE. The MPEF AOD is

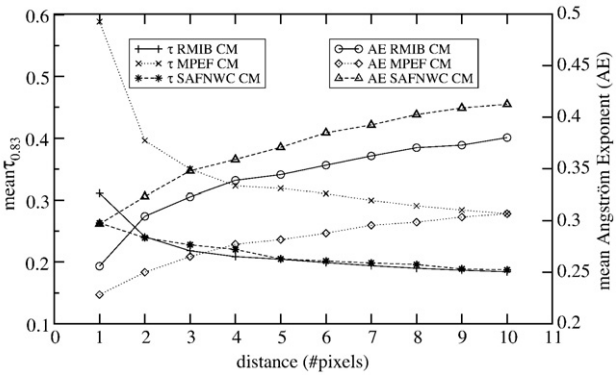

Fig. 4. Mean $\tau_{0.83}$ and mean AE ($\tau_{0.83}$, $\tau_{1.61}$) as a function of proximity to the cloud border for the three CMs. Derived from data on March 6, 2004 at 12:00 UTC shown in Fig. 2.

biased high by ~0.1 away from cloud, and by ~0.2–0.3 in the vicinity of cloud, and AE is biased low by ~0.04–0.08, indicating the largest contamination by residual cloud, among all three products.

Analyses in this section show that the RMIB CM is fairly conservative. The fact that the RMIB CM does not depend on numerical weather prediction (NWP) model output (unlike the SAFNWC CM), may be beneficial for constructing a climate data record. We thus conclude that the RMIB CM can be used to generate a high-quality aerosol product and will continue using it within the RGP project. For the rest of this discussion, only RMIB-based aerosol results are presented and discussed.

4. Results

The high temporal (one full-disk scan every 15 min) and spatial resolution (5-km pixel size, at nadir) allow a much more accurate characterization of aerosols over the entire hemisphere. This section illustrates a new potential to capture seasonal variability in AOD and AE.

4.1. Seasonal mean Aerosol Optical Depth

Fig. 5 maps seasonal mean AOD (0.83 μm) from December 21, 2005 to December 21, 2006. These seasonal maps can be compared

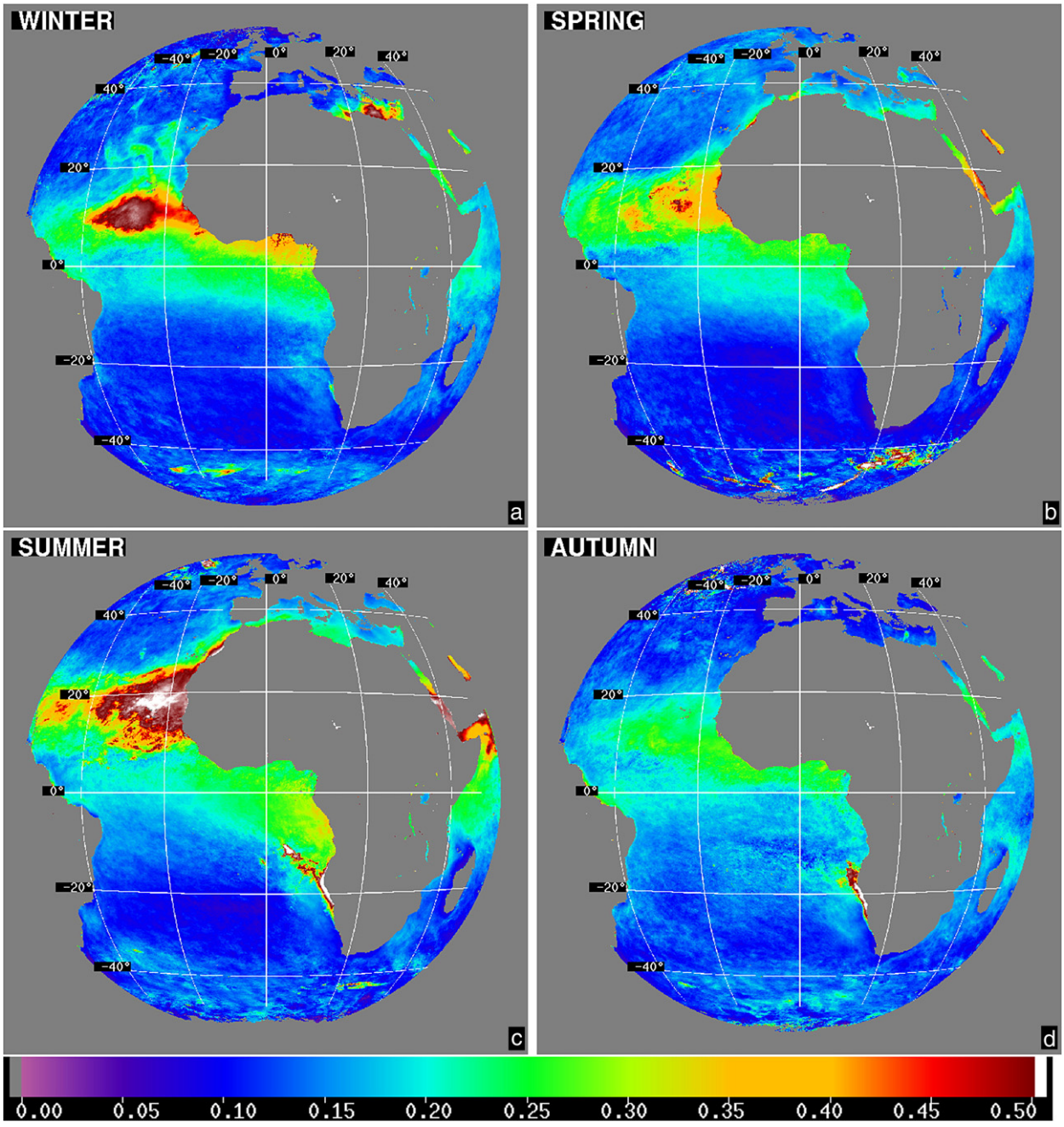

Fig. 5. Seasonal mean SEVIRI AOD at 0.83 μm from: (a) December 21, 2005–March 20, 2006; (b) March 21–June 20, 2006; (c) June 21–September 20, 2006; (d) September 21–December 20, 2006. White areas correspond to AOD>0.5, grey areas indicate no retrievals. Spatial resolution is 9 km.

with their respective counterparts derived from AVHRR/2 onboard NOAA-11 using the previous second generation NESDIS aerosol algorithm, and using a different base period from July 1989 to June 1991 (Husar et al., 1997). Background AOD values over open oceans are $\tau \sim 0.10$. Husar et al. (1997) have observed that "the most prominent areas of increased AOD are associated with continental sources, which are markedly elongated into open oceans in well defined flow fields such as trade winds areas. A second type of AOD deviation from background, consist of isolated patches that do not appear to be linked to continental sources and show much weaker spatial gradients". Comparisons of our Fig. 5 with Plate 1 from Husar et al. (1997) show that the two patterns of AOD distributions are very similar.

During the winter of 2006, the high AOD is observed in the Gulf of Guinea and extending over the subtropical Northern Atlantic due to the biomass burning activity (e.g., Anderson et al., 1996; Dwyer et al., 2000; Loeb et al., 2003). A signal from the Saharan desert dust event in the beginning of March 2006 is superimposed on the biomass burning signal. The increased AOD over the Eastern Mediterranean is due to several dust events over Northern Africa from February 23 to 25, 2006. The AOD is low over the rest of the Mediterranean, and to the north of 30°N over the Northern Atlantic.

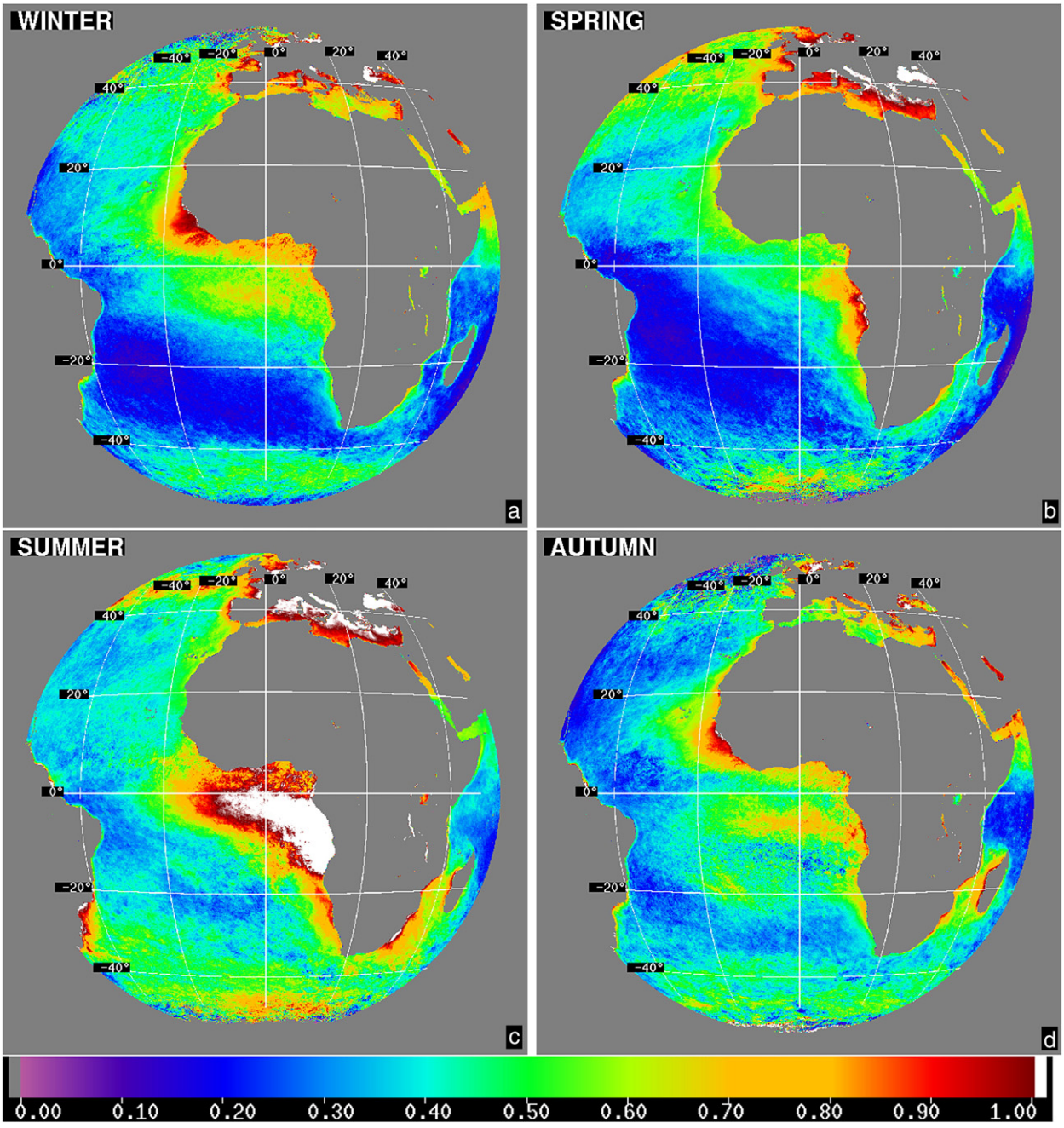

Fig. 6. Seasonal mean AE derived using Eq. (4) from SEVIRI AODs in bands 2 ($\lambda_i = 0.83$ μm) and 3 ($\lambda_j = 1.61$ μm) for the same time intervals as in Fig. 5. White areas correspond to AE > 1.0, and grey areas indicate no retrievals.

In the spring of 2006, the Saharan desert aerosol off the coast of West Africa spreads all over the subtropical Northern Atlantic and reaches the Amazon basin. Similar dust events are responsible for the high AOD over the Red Sea and the Persian Gulf. The AOD is elevated off the coast of West Central Africa, due to increased biomass burning. Note however that the magnitude of the biomass burning AOD may be suppressed, due to the lack of a restoral test for this type of aerosol as described in Section 3.1.

The summer of 2006 is characterized by the maximum amount of mineral aerosols that spread along the Tropic of Cancer over the Northern Atlantic and over the Red Sea and the Gulf of Aden. The parts of the Mediterranean Sea near northern Africa also show increased AOD. In the Southern Hemisphere, high AOD off the Angola coast is linked to a peak in biomass burning activity. Further to the south, very high AOD are observed off the Namib desert. In southwestern Asia, desert storms intensify and now cover most of the Red Sea, the Arabian Sea, and the Persian Gulf.

During the fall of 2006, AOD is at its seasonal minimum in the domain covered by Meteosat-8. Elevated AODs over the Gulf of Guinea and off the west coast of Africa are mostly due to biomass burning, while the flow of the Saharan dust is at its seasonal minimum (Kinne et al., 2003; Yu et al., 2003). The Namib desert continues to contribute to the very high AODs off shore.

For all seasons there are some obvious features close to Antarctic, which are due to a bad scene identification. These pixels are identified as ocean water, but actually they are covered by snow or ice. This problem was recently investigated by Bertrand et al. (2007).

Many of these AOD features have been observed and documented in previous studies. The added value of the SEVIRI AOD product, compared to past and current polar platforms such as NOAA or Terra and Aqua that provide only one look per day, lies in its high spatial and temporal resolution which offers much better potential to resolve mesoscale, regional, and local aerosol events, and to monitor their evolution continuously in time.

4.2. Seasonal distributions of the Ångström Exponent

The multi-spectral potential of SEVIRI allows calculation of the AE using Eq. (4).

$$\alpha_{ij} = -\frac{\ln \frac{\tau\lambda_i}{\tau\lambda_j}}{\ln \frac{\lambda_i}{\lambda_j}} \tag{4}$$

Where τ is the AOD, λ the wavelength, and α the AE. The AE is a good proxy for aerosol particle size. Typically, it ranges from 0 to 2, with small AEs corresponding to large particles (e.g., sea spray or dust), and large AEs corresponding to small particles (e.g., biomass burning or industrial pollution.) The AOD itself cannot provide information about aerosol type.

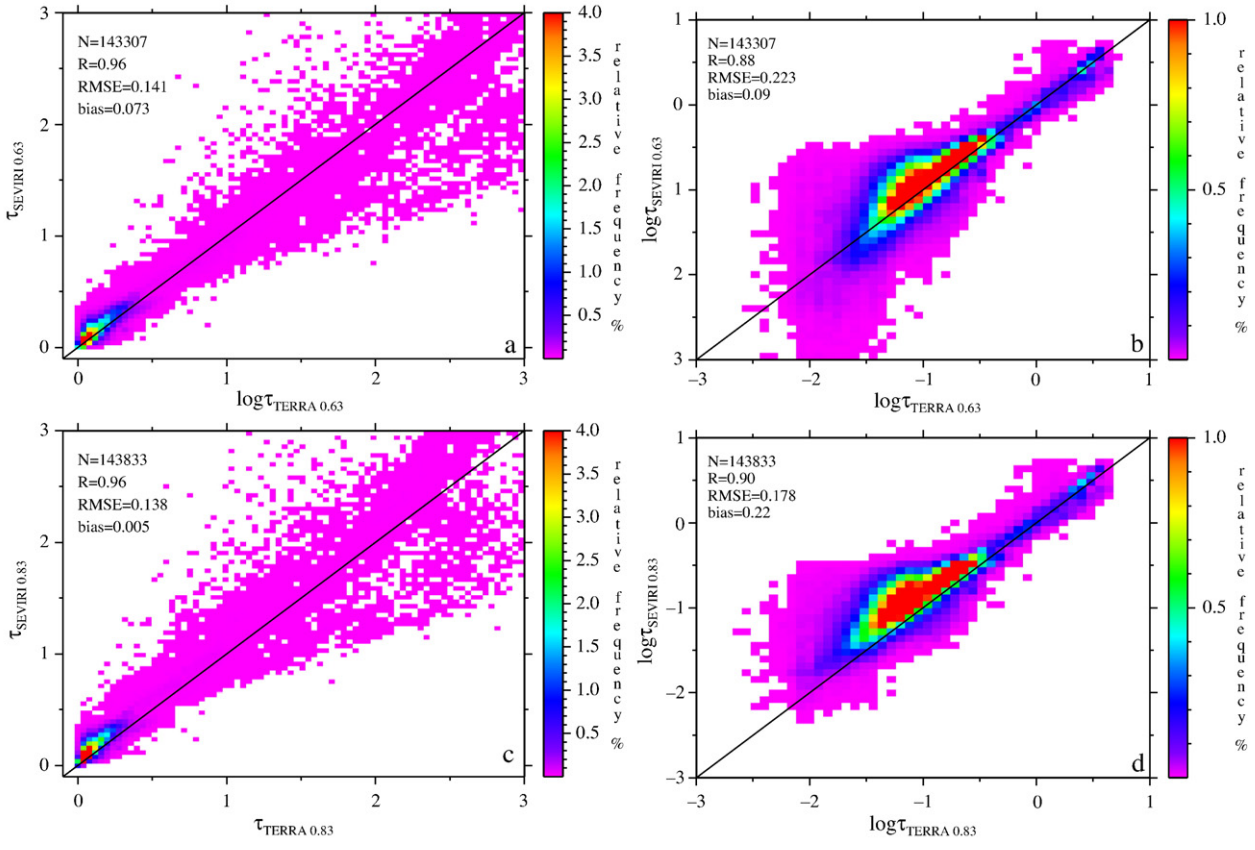

Fig. 7. SEVIRI versus MODIS/Terra density plot derived from February 28 until March 12, 2004: (a) scattergram of SEVIRI $\tau_{0.63}$ versus MODIS/Terra $\tau_{0.63}$; (b) scattergram of SEVIRI $\log(\tau_{0.63})$ versus MODIS/Terra $\log(\tau_{0.63})$; (c) same as (a) but at 0.83 μm; (d) same as (b) but at 0.83 μm.

Attributing elevated AODs to the source done in the previous section (e.g., dust, biomass burning) was solely based on our a priori knowledge, derived from prior studies based on combining satellite and in situ aerosol measurements (e.g., Husar et al., 1997). Using the AE gives insight into the source of different aerosols, although it may not necessarily be complete and unambiguous.

Fig. 6 shows four seasonal distributions of the AE, associated with the respective panels in Fig. 5. The AE was derived from the AODs in SEVIRI bands 2 (0.83 μm) and 3 (1.61 μm). Recall that the AE may depend upon the spectral interval, as particle size distribution does not always obey Junge's law (Junge, 1952). Also, one should keep in mind that AE is very sensitive to any errors in the two AODs, which may result from instrumental (e.g., calibration, radiometric noise) or retrieval model errors (e.g., violation of the assumption on the surface reflection, which currently assumes clear ocean Case 1 waters) (Ignatov et al., 1998). Therefore, this discussion concentrates primarily on the relative values of the AE (spatial distribution and seasonal cycle) rather than absolute AE values, which may be subject to uncertainty.

For the background aerosols in the open oceans (e.g., Southern Atlantic in winter and spring 2006), AE is from ~0.1 to 0.2 (blue in Fig. 6) which corresponds to the undisturbed sea salt. AE is from ~0.3 to 0.5 (light blue to greenish colors) for large dust particles, and >0.7 for biomass burning and industrial pollution. Fig. 6 substantiates the discussion in Section 4.1 when interpreting elevated aerosol features in Fig. 5. For instance, in the winter of 2006 AE is elevated over a large area off the West African Coast from the Gulf of Guinea to Senegal, suggesting that the elevated AOD here is due to biomass burning. On the other hand, the large area of increased AOD in the Central Atlantic in Fig. 5a is due to dust, as corresponding the AE in Fig. 6a is <0.5. Fig. 6 further confirms that the peak biomass burning took place in summer 2006, where a large area off the coast of southwestern Africa shows AE>1. Note also that the AE is elevated along the European coast at all seasons, suggesting that the air pollution comes from the European continent year-round.

Note that the frequent SEVIRI measurements from the same area, with high spatial resolution, are particularly valuable for monitoring the AE, which is a highly noisy parameter and needs averaging over many data points for a reliable estimate (Ignatov et al., 1998).

5. Comparisons with MODIS

To evaluate the global performance of the SEVIRI AOD product, it was compared with the MODIS aerosol product, which is currently considered a standard in the remote sensing community (Remer et al., 2005). Please note that this comparison, although over the entire SEVIRI disk and best available to date still does not provide a conclusive measure of SEVIRI product performance for at least two reasons. First, the comparisons between the two products are obviously biased towards clear skies

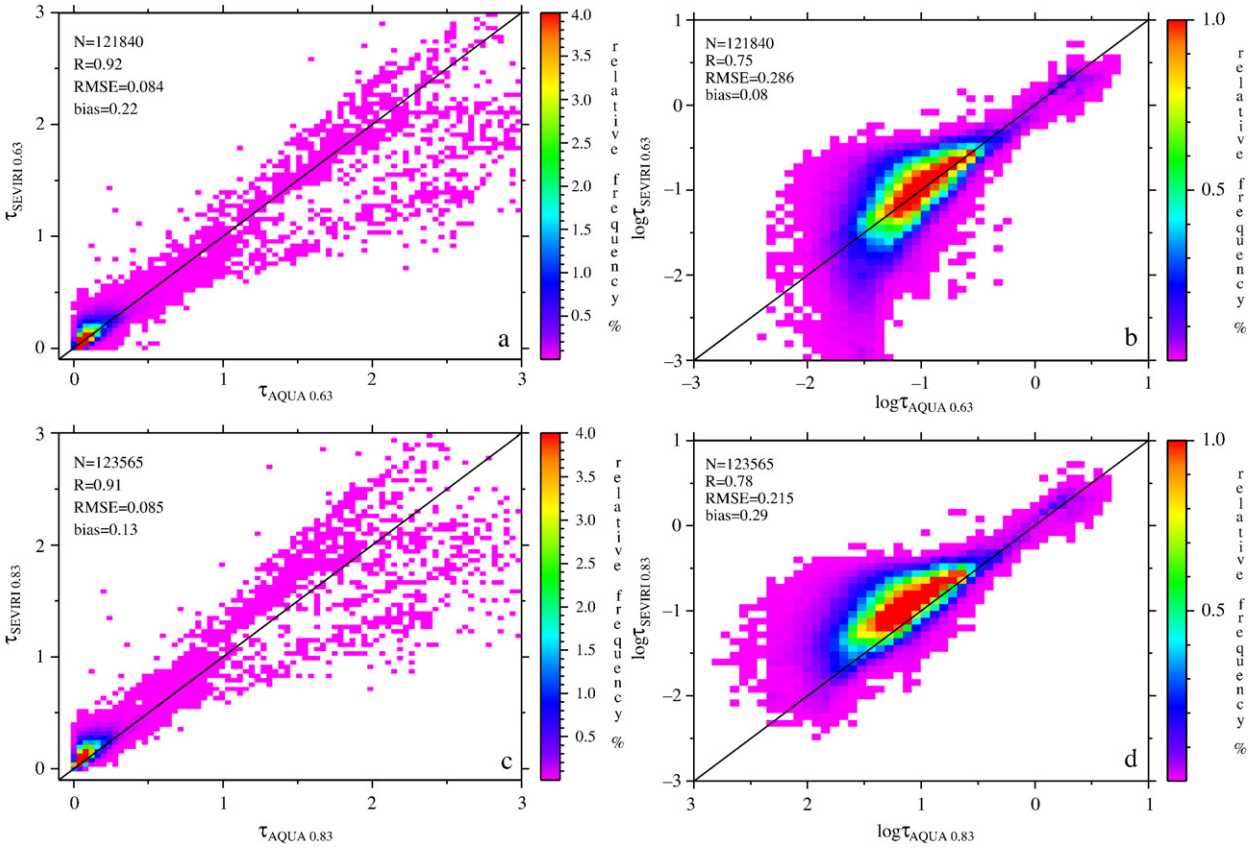

Fig. 8. SEVIRI versus MODIS/Aqua density plot derived from February 28 until March 12, 2004: (a) scattergram of SEVIRI $\tau_{0.63}$ versus MODIS/Aqua $\tau_{0.63}$; (b) scattergram of SEVIRI log($\tau_{0.63}$) versus MODIS/Aqua log($\tau_{0.63}$); (c) same as (a) but at 0.83 μm; (d) same as (b) but at 0.83 μm.

as each 10-km box used in the comparisons was identified as cloud-free by both MODIS and SEVIRI cloud screening. No attempt was made here to quantify performance of the SEVIRI aerosol retrievals in those pixels which were identified as cloudy by the MODIS CM. Also, when using the MODIS aerosol product as a validation standard, one should keep in mind that it was only evaluated against several AERONET coastal and island stations, which may not be globally representative and, therefore, may not fully quantify its global performance.

MODIS spectral AOD is derived from two polar satellites, Terra and Aqua, and reported on the MOD04/L2 (for Terra) and MYD04/L2 (for Aqua) data sets. To account for the minor differences in the reference wavelengths between MODIS and SEVIRI in the current comparisons, the MODIS AODs (reported at wavelengths of 0.644, and 0.855 μm) were scaled to the nearest SEVIRI AODs (reported at 0.630, and 0.830 μm) using an Ångström fit as described by Eq. (1).

To match the 10-km resolution of M*D04 data, the 15-minute SEVIRI measurements closest in time to MODIS were averaged over 3×3 pixels and merged with M*D04 by minimizing the distance between the respective centers of the ~10-km boxes. A 14-day data set from February 28, 2004 to March 12, 2004 was selected for comparisons, which provides sufficient statistics of correlation between SEVIRI and MODIS and spans a globally representative range of aerosol types and loadings and retrieval conditions (ambient cloud and sun-view illumination geometries).

The left panels of Fig. 7 show the SEVIRI AODs in 2 bands against their respective Terra MODIS counterparts, and the right panels of Fig. 7 show the same data but in a log–log scale. The data are more regularly distributed in a log–log space, due to a log–normal nature of AOD, and therefore easier to analyze (Ignatov et al., 2006). Fig. 8 is similar to Fig. 7, except it uses Aqua rather than Terra MODIS AOD data on the *x*-axis.

The correlation between the SEVIRI and MODIS AODs is ~0.96 for Terra and ranges from ~0.91 to 0.92 for Aqua, the range representing band-to-band variations. SEVIRI AOD correlates better with Terra than with Aqua, although it is not immediately clear why. The correlation is weaker in a log scale than in the linear scale (~0.88 to 0.90 for Terra and ~0.75 to 0.78 for Aqua), due to large variations in SEVIRI low-end AODs, which in turn are likely due to larger radiometric noise in SEVIRI data compared to MODIS. Note that a log-transformation amplifies all additive errors in AODs, especially at low-end AOD.

Another prominent feature of Figs. 7 and 8 is a positive bias in SEVIRI AODs 0.83 μm, relative to MODIS. This bias appears to be uniform in the full range of AODs and thus unlikely due to the NESDIS aerosol model which, according to the analyses in Fig. 1, may even be biased low at high AODs. Ignatov et al. (2006) observed a small positive bias (from ~+0.003 to 0.011) in AVHRR-like single channel retrievals from MODIS radiances, compared to M*D04 AOD. Cloud screening was also different in the two products. They attributed approximately half of this bias to the differences between M*D04 and NESDIS aerosol

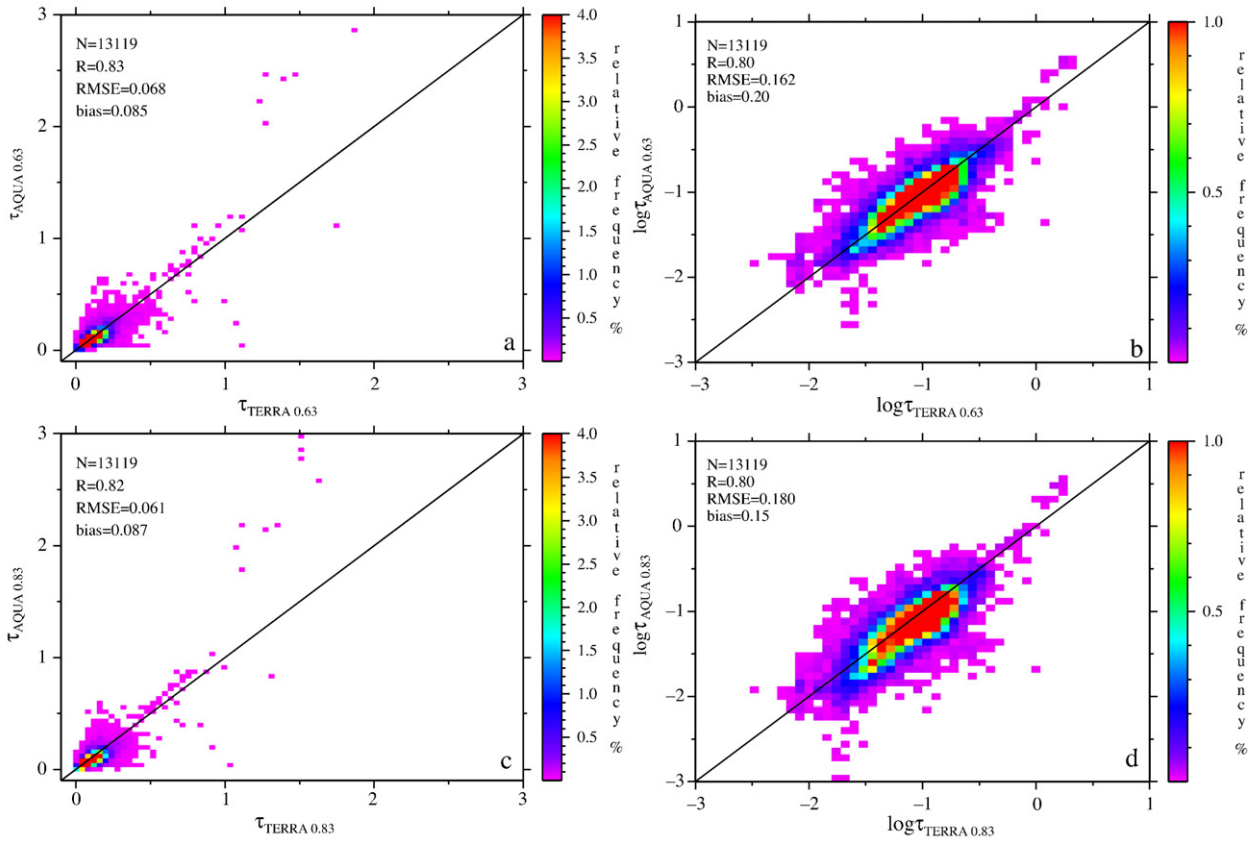

Fig. 9. MODIS/Terra versus MODIS/Aqua density plot derived from February 28 until March 12, 2004: (a) scattergram of MODIS/Terra $\tau_{0.63}$ versus MODIS/Aqua $\tau_{0.63}$; (b) scattergram of MODIS/Terra log($\tau_{0.63}$) versus MODIS/Aqua log($\tau_{0.63}$); (c) same as (a) but at 0.83 μm; (d) same as (b) but at 0.83 μm.

models, whereas the other half or so was deemed due to the differences in cloud screening. Note that Ignatov et al. (2006) analyzed M*D04 collection 4, and only retrievals in MODIS band 1 centered at 0.644 μm (counterpart to SEVIRI band 1).

Uncertainties in the SEVIRI radiances are another potential source of the high biases in the SEVIRI AODs in band 2. Until now, the accuracy of the SEVIRI vicarious calibration has not been assessed independently.

To quickly check for possible biases between the two MODIS instruments used in these comparisons, Fig. 9 plots Terra versus Aqua AOD. The 10-km boxes being compared can be separated by more than 3 h, which can cause extra noise. The density plots are centered along the 45° line, both in the linear and in log–space. The observed spread is partly due to the large temporal matching range, and the Terra-Aqua correlation generally compares favorably with the SEVIRI-Terra and SEVIRI-Aqua numbers. Aqua AODs tend to be biased somewhat low compared to the Terra AODs, with bias being smallest at 0.63 μm and progressively increasing towards longer wavelengths.

Overall, comparisons with MODIS suggest that the SEVIRI aerosol product is reasonable, although it shows somewhat more noise and unexplained high biases in the two long wave bands. Both these factors would particularly affect the aerosol size parameter estimate and should be addressed in the future revisions of the RGP aerosol product.

6. Example of using the aerosol product for aerosol forcing estimates

The major motivation for including an aerosol product in the RGP is the analysis of the direct radiative effect of aerosols. As a preliminary example of such analyses, Fig. 10 shows a monthly average cloud-free reflected solar flux derived from the GERB observations (version V3) for March 2004. This month was characterized by a significant dust event. The GERB fluxes in the glint area are not defined and therefore not included in the average. However, the artifacts (stripes) north of the equator correspond to the remaining sun glint.

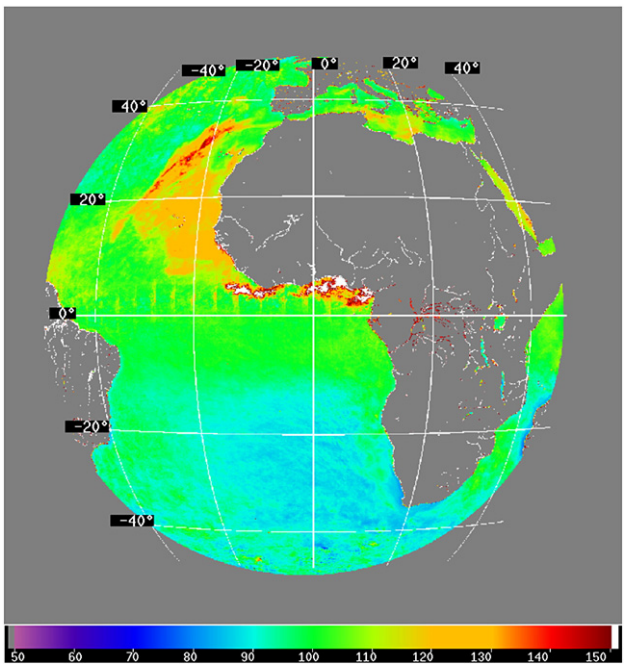

Fig. 10. Mean short wave cloud-free flux (W m^{-2}) for March 2004. The grey areas correspond to land surface.

Only clear sky GERB pixels were selected for this analysis, using the RMIB CM. However, the white areas in the Gulf of Guinea may still be contaminated by residual cloud because estimation of clear sky values in this region is difficult due to the persistent cloud in the Inter-Tropical Convergence Zone. This area is also characterized by biomass burning activity all year-round. Concentrating on the ocean area to the west of the Sahara, one observes a large homogeneous patch that is characterized by an elevated solar flux. This area was characterized by an increased concentration of dust aerosols between March 5 and March 10 (cf. Fig. 3a). For increasing AOD the corresponding short wave flux increases due to the enhanced reflection of the solar radiation by the aerosols. The dust-affected reflected solar fluxes measure around 125 W m^{-2} (orange color west of the Sahara), whereas the background reflected solar flux values are around 85 W m^{-2} (blue color) in the southern Atlantic, west of South Africa. From comparison of these results, a simple estimate of a monthly mean direct radiative forcing due to desert dust is thus as high as 40 W m^{-2}.

7. Conclusions

The new RGP product has spectral AOD at 0.63, 0.83and 1.61 μm to be used with the GERB fluxes to estimate the direct radiative effect of aerosols. The aerosol algorithm and its implementation for SEVIRI are described in Brindley and Ignatov (2006). For the RGP, the algorithm was implemented independently and operationally applied to much larger data sets. Its validation for confidently clear sky pixels shows that SEVIRI retrievals closely replicate the full diurnal cycle measured by AERONET. The accuracy of SEVIRI AOD is comparable with MODIS AOD, with SEVIRI providing 15-minute sampling of aerosol compared to once-a-day samples from MODIS.

The unphysical single channel retrieval algorithm differs from the algorithms used in other satellite data analyses ((Higurashi et al., 2000; Mishchenko et al., 1999; Remer et al., 2005)). Premises of using a simple and robust algorithm with AVHRR data have been extensively discussed in Ignatov et al. (2004) (see their Conclusion section) and other peer-reviewed publications referenced therein.

In real time processing, AVHRR calibration uncertainties lead to a fundamental instability of the estimating aerosol model under typical maritime conditions. Ignatov et al. (2004) thus conclude that robust single channel retrievals should be continued in the NOAA operations, and more sophisticated multi-channel techniques should be deferred to reprocessing historical AVHRR data, in which sensor calibration uncertainties have a better chance to be contained. Recall that SEVIRI is an AVHRR-like sensor, which also lacks an on-orbit calibration device and is therefore calibrated vicariously. Ignatov et al. (2004) have

shown that anomalies in single channel aerosol product are directly related to calibration errors in input radiances. Small biases in SEVIRI AODs with respect to MODIS AODs observed in channels 2 and 3 are deemed to be mainly due to residual SEVIRI calibration uncertainties. Detailed analyses of this observation are beyond the scope of this study.

On the other hand, when a single channel algorithm retrieval algorithm is applied to well-calibrated satellite radiances such as from MODIS, then the AVHRR-like retrieval algorithm produces results which are largely consistent with more sophisticated MOD04 algorithm, and validates against AERONET comparably to more sophisticated algorithms ((Ignatov et al., 2005; Brindley & Ignatov, 2006; Myhre et al., 2004; Smirnov et al., 2006); this study). We thus conclude that at this stage, the single channel NESDIS aerosol algorithm is fully consistent with the SEVIRI data. It can be used to detect problems with input radiances, but provides a reasonable estimate of aerosol properties over oceans when radiances are accurate. Furthermore, a single channel product provides a benchmark, against which all subsequent multi-channel improvements can be measured.

The RGP uses a simple RMIB CM, which was compared with the MPEF CM and the SAFNWC CM and proves to be simple yet conservative. Inaccurate cloud screening is a major problem for aerosol remote sensing since the indirect aerosol effect in the vicinity of clouds causes significant uncertainties in the retrieved AOD. More research is needed to define accurate cloud screening strategies, but the RMIB CM can be used to generate a high-quality aerosol product and will continue to be used within the RGP. The major area for the RMIB CM improvement is the development of restoral tests for non-dust aerosol with high AOD, which may be currently screened out by the overly conservative RMIB CM.

More than one year of AOD has been processed from SEVIRI, which allows monitoring of the temporal and regional distribution of aerosols in the Meteosat domain. Newly generated seasonal AOD maps for the year 2006 correspond to the aerosol distribution reported by previous studies. The multi-spectral nature of the SEVIRI AOD retrievals allows calculation of an Ångström Exponent representative of particle size. This calculation gives insight into the source of aerosols that can be linked to the regional sources of desert dust and biomass burning from Africa and industrial pollution from Europe.

In addition to its multi-spectral nature, the value of the SEVIRI aerosol product is in its high spatial and temporal resolution, which offer a much better potential to resolve mesoscale, regional, and local aerosol events, and monitor their evolution continuously in time.

The comparison with the MODIS aerosol product shows a very close agreement, with the SEVIRI AODs being somewhat more noisy compared to MODIS and biased high in short wave band 2 (0.83 μm).

Finally, we provide an example of the aerosol data usage to estimate the direct radiative effect of dust in March 2004. The mean short wave fluxes increase with increasing mean AODs, due to the enhanced reflection of the solar radiation by the aerosols, resulting in a monthly mean direct radiative forcing of 40 W m^{-2} over the ocean west of the Sahara for March 2004. The high temporal resolution of SEVIRI and GERB allows derivation of a continuous record of the direct aerosol forcing. In addition to the high spatial resolution, differences in forcing can be observed on a wide range of scales, from local to mesoscale spatially and from 15 min to months and years temporally. This observation, however, requires a thorough analysis of a large data set, which is reserved for future work.

References

Anderson, B. E., Grant, W. B., Gregory, G. L., Browell, E. V., Collins, J. E., Jr., Sachse, G. W., et al. (1996). Aerosols from biomass burning over the tropical South Atlantic region: Distribution and impacts. *Journal of Geophysical Research*, *101*, 24117–24137.

Bertrand, C., Gonzalez, L., Ipe, A., Clerbaux, N., & Dewitte, S. (2007). Improvement in the GERB short wave flux estimations over snow covered surfaces. *Advances in Space Research*. doi:10.1016/j.asr.2006.12.016

Brindley, H., & Ignatov, A. (2006). Retrieval of mineral aerosol optical depth and size information from Meteosat Second Generation SEVIRI solar reflectance bands. *Remote Sensing of Environment*, *102*, 344–363.

Brindley, H., & Russel, J. (2006). Improving GERB scene identification using SEVIRI: Infra-red dust detection strategy. *Remote Sensing of Environment*, *104*, 426–446.

Coakley, J. A., & Walsch, C. D. (2002). Limits to the Aerosol Indirect Radiative Effect Derived from Observations from Ship Tracks. *Journal of the Atmospheric Sciences*, *59*, 668–680.

Derrien, M., & Le Gléau, H. (2005). MSG/SEVIRI cloud mask and type from SAFNWC. *International Journal of Remote Sensing*, *26*, 4707–4732.

Dewitte, S., Gonzalez, L., Clerbaux, N., Ipe, A., Bertrand, C., & De Paepe, B. The Geostationary Earth Radiation Budget Edition 1 Data processing algorithms, Advances in Space Research, accepted for publication. doi:10.1016/J.asr.2007.07.042

Dwyer, E., Pinnock, S., & Grégoire, J. -M. (2000). Global spatial and temporal distribution of vegetation fire as determined from satellite observations. *International Journal of Remote Sensing*, *21*, 1289–1302.

Govaerts, Y., & Clerici, M. (2004). MSG-1/SEVIRI solar channels calibration commisioning activity report, EUMETSAT, EUM/MSG/TEN/04/2004, available from http://www.eumetsat.int

Harries, J. E., Russel, J. E., Hanafin, J. A., Brindley, H., Futyan, J., Rufus, J., et al. (2005). The Geostationary Earth Radiation Budget Project. *Bulletin of American Meteorological Society*, *86*, 945–960.

Higurashi, A., Nakajima, T., Holben, B. N., Smirnov, A., Frouin, R., & Chatenet, B. (2000). A Study of Global Aerosol Optical Climatology with Two-Channel AVHRR Remote Sensing. *Journal of Climate*, *13*, 2011–2027.

Husar, R., Prospero, J., & Stowe, L. (1997). Characterization of tropospheric aerosols over the oceans with the NOAA AVHRR optical thickness operational product. *Journal of Geophysical Research*, *102*(D14), 16889–16909.

Ignatov, A., Minnis, P., Loeb, N., Wielicki, B., Miller, W., Sun-Mack, S., et al. (2005). Two MODIS aerosol products over ocean on the Terra and Aqua CERES SSF datasets. *Journal of the Atmospheric Sciences*, *62*, 1008–1031.

Ignatov, A., Minnis, P., Miller, W. F., Wielicki, B. A., & Remer, L. (2006). Consistency of global MODIS Aerosol Optical Depths over ocean on Terra and Aqua CERES SSF Datasets. *Journal of Geophysical Research*, *111*, D14202. doi:10.1029/2005JD006645

Ignatov, A., Sapper, J., Cox, S., Laszlo, I., Nalli, N. R., & Kidwell, K. B. (2004). Operational Aerosol Observations (AEROBS) from AVHRR/3 On Board NOAA-KLM Satellites. *Journal of Atmospheric and Oceanic Technology*, *21*(1), 3–26.

Ignatov, A., & Stowe, L. (2002). Aerosol Retrievals from Individual AVHRR Channels. Part I: Retrieval Algorithm and Transition from Dave to 6S Radiative Transfer Model. *Journal Atmospheric Sciences*, *59*(3), 313–334.

Ignatov, A., Stowe, L., & Singh, R. (1998). Sensitivity study of the Angstrom exponent derived from AVHRR over the oceans. *Advances in Space Research*, *21*(3), 439–442.

Ipe, A., Clerbaux, N., Bertrand, C., Dewitte, S., & Gonzalez, L. (2003). Pixel-scale composite top-of-the-atmosphere clear-sky reflectances for Meteosat-7 visible data. *Journal of Geophysical Research*, *108*(D19), 4612. doi:10.1029/2002JD002771

Ipe, A., Bertrand, C., Clerbaux, N., Dewitte, S., & Gonzalez, L. (2004). Validation and homogenisation of cloud optical depth and cloud fraction retrievals for GERB/SEVIRI scene identification using Meteosat-7 data. *Atmospheric Research*, *72*, 17−37.

Junge, C. E. (1952). Gesetzmazigkeiten in der Grozenverteilung atmospharischer Aerosole uber dem Kontinent. *Ber. D. Wetterd. US-Zone*, *35*, 261−277.

Key, J., & Schweiger, A. J. (1998). Tools for atmospheric radiative transfer: Streamer and FluxNet. *Computers & Geosciences*, *24*, 443−451.

King, M. D., Kaufman, Y. J., Tanré, D., & Nakajima, T. (1999). Remote Sensing of Tropospheric Aerosols from Space: Past, Present, and Future. *Bulletin American Meteorological Society*, *80*, 2229−2259.

Kinne, S., Lohmann, U., Feichter, J., Schulz, M., Timmreck, C., Ghan, S., et al. (2003). Monthly averages of aerosol properties: A global comparison among models, satellite data, and AERONET ground data. *Journal of Geophysical Research*, *108*(D20), 4634. doi:10.1029/2001JD001253

Loeb, N. G., & Kato, S. (2002). Top-of-Atmosphere Direct Radiative Effect of Aerosols over the Tropical Oceans from the Clouds and the Earth's Radiant Energy System (CERES) Satellite Instrument. *Journal Climate*, 1474−1484.

Loeb, N. G., Smith, N. M., Kato, S., Miller, W. F., Gupta, S., Minnis, P., et al. (2003). Angular distribution modelsfor top-of-atmosphere radiative flux estimation from the Clouds and the Earth's Radiant Energy System instrument on the Tropical Rainfall Measuring Mission Satellite. part I: Methodology. *Journal Applied Meteorology*, *42*, 240−265.

Lutz, H. (1999). Cloud processing for METEOSAT second generation, EUMETSAT, Technical Memorandum, vol. 4, Darmstadt, Germany.

Matheson, M. A., Coakley, J. A., & Tahnk, W. R. (2005). Aerosol and cloud property relationships for summertime stratiform clouds in the northeastern Atlantic from Advanced Very High Resolution Radiometer observations. *Journal of Geophysical Research*, *110*, D24204. doi:10.1029/2005JD006165

Meteorological Products Extraction Facility. (2007). Cloud Detection for MSG - Algorithm Theoretical Basis Document, EUMETSAT, 2007, EUM/MET/REP/07/0132, available from http://www.eumetsat.int

Mishchenko, M. I., Geogdzhayev, I. V., Cairns, B., Rossow, W. B., & Lacis, A. A. (1999). Aerosol retrievals over the ocean by use of channels 1 and 2 AVHRR data: Sensitivity analysis and preliminary results. *Applied Optics*, *38*, 7325−7341.

Myhre, G., Stordal, F., Johnsrud, M., Ignatov, A., Mishchenko, M. I., Geogdzhayev, I. V., et al. (2004). Intercomparison of Satellite Retrieved Aerosol Optical Depth over the Ocean. *Journal of the Atmospheric Sciences*, *61*, 499−513.

Nakajima, T. Y., & King, M. D. (1990). Determination of the optical thickness and effective particle radius of clouds from reflected solar radiation measurements. Part I: Theory. *Journal of Atmospheric Science*, *47*, 1878−1893.

Nakajima, T. Y., & Nakajima, T. (1995). Wide-area determination of cloud microphysical properties from NOAA AVHRR measurements for FIRE and ASTEX regions. *Journal of Atmospheric Science*, *52*, 4043−4059.

Remer, L. A., Kaufman, Y. J., Tanre, D., Mattoo, S., Chu, D. A., Martins, J. V., et al. (2005). The MODIS Aerosol Algorithm, Products, and Validation. *Journal of the Atmospheric Sciences-Special Section*, *62*, 947−973.

Schmetz, J., Pili, P., Tjemkes, S., Just, D., Kerkmann, J., Rota, S., et al. (2002). An Introduction to Meteosat Second Generation. *Bulletin American Meteorological Society*, *83*, 977−992.

Smirnov, A., Holben, B. N., Eck, T. F., Dubovik, O., & Slutsker, I. (2000). Cloud-Screening and Quality Control Algorithms for the AERONET Database. *Remote Sensing of Environment*, *82*, 337−349.

Smirnov, A., Holben, B. N., Sakerin, S. M., Kabanov, D. M., Slutsker, I., Chin, M., et al. (2006). Ship-based aerosol optical depth measurements in the Atlantic Ocean: Comparison with satellite retrievals and GOCART model. *Geophysical Research Letters*, *33*, L14817. doi:10.1029/2006GL026051

Wen, G., Marshak, A., & Cahalan, R. F. (2006). Impact of 3-D Clouds on Clear-Sky Reflectance and Aerosol Retrieval in a Biomass Burning Region of Brazil. *IEEE Geoscience and Remote Sensing Letters*, *3*, 169−172.

Wielicki, B. A., Barkstrom, B. R., Harrison, E. F., Lee, R. B., III, Smith, G. L., & Cooper, J. E. (1996). Clouds and the Earth's Radiant Energy System (CERES): An Earth Observing System Experiment. *Bulletin of the American Meteorological Society*, *77*, 853−868.

Yu, H., Dickinson, R. E., & Chin, M. (2003). Annual cycle of global distributions of aerosol optical depth from integration of MODIS retrievals and GOCART model simulations. *Journal of Geophysical Research*, *108*(D3), 4128. doi:10.1029/2002JD002717